RESEARCH ARTICLE

NANO · MICRO small
www.small-journal.com

# Visualizing Ribbon-to-Ribbon Heterogeneity of Chemically Unzipped Wide Graphene Nanoribbons by Silver Nanowire-Based Tip-Enhanced Raman Scattering Microscopy

*Tomoko Inose, Shuichi Toyouchi,* Shinnosuke Hara, Shoji Sugioka, Peter Walke, Rikuto Oyabu, Beatrice Fortuni, Wannes Peeters, Yuki Usami, Kenji Hirai, Steven De Feyter, Hiroshi Uji-i, Yasuhiko Fujita,* and Hirofumi Tanaka**

**Graphene nanoribbons (GNRs), a quasi-one-dimensional form of graphene, have gained tremendous attention due to their potential for next-generation nanoelectronic devices. The chemical unzipping of carbon nanotubes is one of the attractive fabrication methods to obtain single-layered GNRs (sGNRs) with simple and large-scale production. The authors recently found that unzipping from double-walled carbon nanotubes (DWNTs), rather than single- or multi-walled, results in high-yield production of crystalline sGNRs. However, details of the resultant GNR structure, as well as the reaction mechanism, are not fully understood due to the necessity of nanoscale spectroscopy. In this regard, silver nanowire-based tip-enhanced Raman spectroscopy (TERS) is applied for single GNR analysis and investigated ribbon-to-ribbon heterogeneity in terms of defect density and edge structure generated through the unzipping process. The authors found that sGNRs originated from the inner walls of DWNTs showed lower defect densities than those from the outer walls. Furthermore, TERS spectra of sGNRs exhibit a large variety in graphitic Raman parameters, indicating a large variation in edge structures. This work at the single GNR level reveals, for the first time, ribbon-to-ribbon heterogeneity that can never be observed by diffraction-limited techniques and provides deeper insights into unzipped GNR structure as well as the DWNT unzipping reaction mechanism.**

## 1. Introduction

Graphene nanoribbons (GNRs), a quasi-one-dimensional form of graphene, have attracted great attention for both fundamental research and nanoelectronic device applications due to the chemical tunability of their band structure.[1–7] GNRs have been produced in a number of methods ranging from top-down[8–14] to bottom-up.[15,16] Bottom-up fabrication allows for the precise design of GNRs based on chemical reaction procedures, resulting in uniform, high-quality nanoribbons. Bottom-up GNRs with nanometer-wide ribbons are appropriate for semiconductor device applications. It also enables the fabrication of nanoribbons with desired functionality by nitrogen atom doping[17] and edge structure control.[18]

Chemical unzipping carbon nanotube (CNT) is another well-studied process in GNR synthesis. The chemical unzipping method produces a reasonably easy GNR synthesis procedure that is ideal for large-scale synthesis.[10–14,19] Typically, the

T. Inose, H. Uji-i
Institute for Integrated Cell-Material Sciences (WPI-iCeMS)
Kyoto University
iCeMS Research Bldg, Yoshida, Sakyo-ku, Kyoto 606–8501, Japan

The ORCID identification number(s) for the author(s) of this article can be found under https://doi.org/10.1002/smll.202301841



**DOI: 10.1002/smll.202301841**

S. Toyouchi, P. Walke, B. Fortuni, W. Peeters, S. De Feyter, H. Uji-i, Y. Fujita
Departement Chemie
KU Leuven
Celestijnenlaan 200F, Heverlee 3001, Belgium
E-mail: shuichitoyouchi@omu.ac.jp; yasuhiko.fujita@aist.go.jp

S. Toyouchi
Research Institute for Light-induced Acceleration System (RILACS)
Osaka Metropolitan University
1–2 Gakuen-cho, Naka-ku, Sakai, Osaka 599–8570, Japan

S. Hara, R. Oyabu, Y. Usami, H. Tanaka
Graduate School of Life Science and Systems Engineering
Kyushu Institute of Technology
2–4 Hibikino, Wakamatsu, Kitakyushu 808-0196, Japan
E-mail: tanaka@brain.kyutech.ac.jp

unzipping process yields GNRs with widths more than 10 nm, with semimetallic properties and the potential for use in nanowiring electronic devices. Unzipped GNRs can be chemically functionalized to add semiconductive characteristics.[20] During chemical unzipping, the quality of the produced GNR is known to be highly dependent on the reaction protocol and/or starting CNT types. In typical cases, CNTs are first oxidized to induce $sp^3$-type defects on the surface, then dispersed in a solution containing dispersing agent/radical sources, and finally unzipped by sonication.[21] We have recently found that the unzipping of double-walled carbon nanotubes (DWNTs), rather than single- or multi-walled, results in high-yield production of crystalline single-layered GNRs (sGNRs) with a relatively short sonication time (e.g., 20 h for SWNTs and 5 h for DWNTs), in which poly(*m*-phenylenevinylene-*co*-2,5-dioctoxy-*p*-phenylenevinylene) (PmPV) acts as both an efficient dispersing agent and radical sources.[20,22,23] Regarding the mechanism of DWNT unzipping, it is observed from atomic force microscopy (AFM) that double-layered GNRs (dGNRs) are first generated, with subsequent sonication leading to the separation of the two graphene layers to form sGNRs. Complementary evidence of this can be found from the presence of partially branched intermediate state GNRs (i.e., y-shaped GNRs) at an early reaction stage (sonication time ≈1 h). Despite this, the detailed characterization of the produced GNRs has yet to be achieved. Raman spectroscopy can be a suitable candidate for this as its vibrational spectrum provides rich information on the chemical and electronic structure of nanocarbons.[24–30] However, the low spatial resolution of Raman spectroscopy (i.e., several hundreds of nanometers) hinders the possibility of the single GNR analysis. Given the expected heterogeneity, nano-Raman spectroscopy is now highly required for further understanding of chemical/electronic structure as well as unzipping reaction mechanisms.

Here, we applied tip-enhanced Raman scattering (TERS) microscopy for single-unzipped GNR analysis. TERS microscopy is known as a powerful technique, which combines the high information content afforded by optical techniques with the molecular level topographic information provided by scanning probe microscopy (SPM).[31–35] Our group has recently developed a novel atomic-force microscopy-based TERS (AFM-TERS) probe by functionalizing chemically synthesized silver nanowires to a standard silicon AFM cantilever.[36–39] High TERS mapping stability as well as extremely high sensitivity aided by the silver nanowires allows us to map out a sample's nanoscale properties, such as defect characterizations on single CNTs below 10 nm resolution.[36–39]

In this paper, we attempt to characterize ribbon-to-ribbon heterogeneity of DWNT unzipped GNRs (ribbon width: 10–40 nm) in terms of defect density and edge structure, focusing on the early unzipping reaction stage (1 h sonication). We report a large variety in defect densities that originates from the difference in radical-attack history between the inner and outer walls of DWNTs, as confirmed via TERS measurement on an intermediate state of GNR (y-shaped GNR). We also consider that unzipped GNRs have a large variation in edge structures. This is based on Raman spectroscopy parameters including the intensity ratio of D-band to G-band and/or G-band peak positions. This work at the single GNR level, for the first time, reveals a large ribbon-to-ribbon heterogeneity that can never be observed by diffraction-limited resolution methods, providing deeper insight into the structure of unzipped GNRs and the reaction mechanism of DWNT unzipping.

## 2. Results and Discussion

### 2.1. AFM Characterizations

First, we demonstrate that GNR and DWNT can be distinguished by AFM topography. **Figure 1**a–c shows typical AFM height images of a single-layered GNR (sGNR), a double-layered GNR (dGNR), and a DWNT, respectively. GNRs were prepared by the DWNT unzipping method previously reported by our group.[20] This produces GNRs with a width range of 10–40 nm without bandgap opening (metallic) or chemical doping. The sample for TERS measurements was prepared by drop-casting a GNR solution of 1 h sonication time onto an Au(111) substrate (see the Experimental Section for details). A short sonication time was targeted as the sample contains multiple types of GNRs (i.e., sGNR, dGNR, etc.) as well as ribbons with intermediate states (y-shaped GNR).[20] We observed carbon nanostructures with three ranges of AFM height: 0.7 nm (d), 1.5 nm (e), and higher than 2 nm (f). As no carbon structure less than 1 nm in height was observed from the original materials (Figure S1, Supporting Information), the observed structure of 0.7 nm can be safely assigned to unzipped sGNRs. The height histogram in Figure 1g shows that sGNRs are a major component of the sample used in this experiment. Also, we barely observed GNRs where two sGNRs are gathered into one ribbon (i.e., bi-layered) with the bi- and single-layered regions, respectively, showing a height of around 1.5 and 0.7 nm (e.g., Figure S2, Supporting Information). Such structure type can be assigned to GNRs of an intermediate state during the unzipping process,[20] which is called y-shaped GNR (yGNR). Accordingly, the structure of 1.5 nm height can be assigned to dGNR. The structure of >2 nm has typically a sharper height profile than GNRs and can be assigned to residual DWNTs (or DWNT bundles). As stated above, the type of CNT or GNRs in the sample can be distinct by AFM topography.

S. Sugioka, K. Hirai, H. Uji-i
Research Institute for Electronic Science (RIES)
Hokkaido University
N20W10, Sapporo 001–0020, Japan
P. Walke
Department of Materials and Environmental Technology
Tallinn University of Technology
Ehitajate tee 5, Tallinn 19086, Estonia
Y. Usami, H. Tanaka
Research Center for Neuromorphic AI Hardware
Kyushu Institute of Technology
2–4 Hibikino, Wakamatsu, Kitakyushu 808-0196, Japan
Y. Fujita
Toray Research Center
Inc.
Sonoyama 3-3-7, Otsu, Shiga 520–8567, Japan
Y. Fujita
Research Institute for Sustainable Chemistry
National Institute of Advanced Industrial Science and Technology (AIST Chugoku)
Kagamiyama 3-11-32, Higashihiroshima, Hiroshima 739-0046, Japan

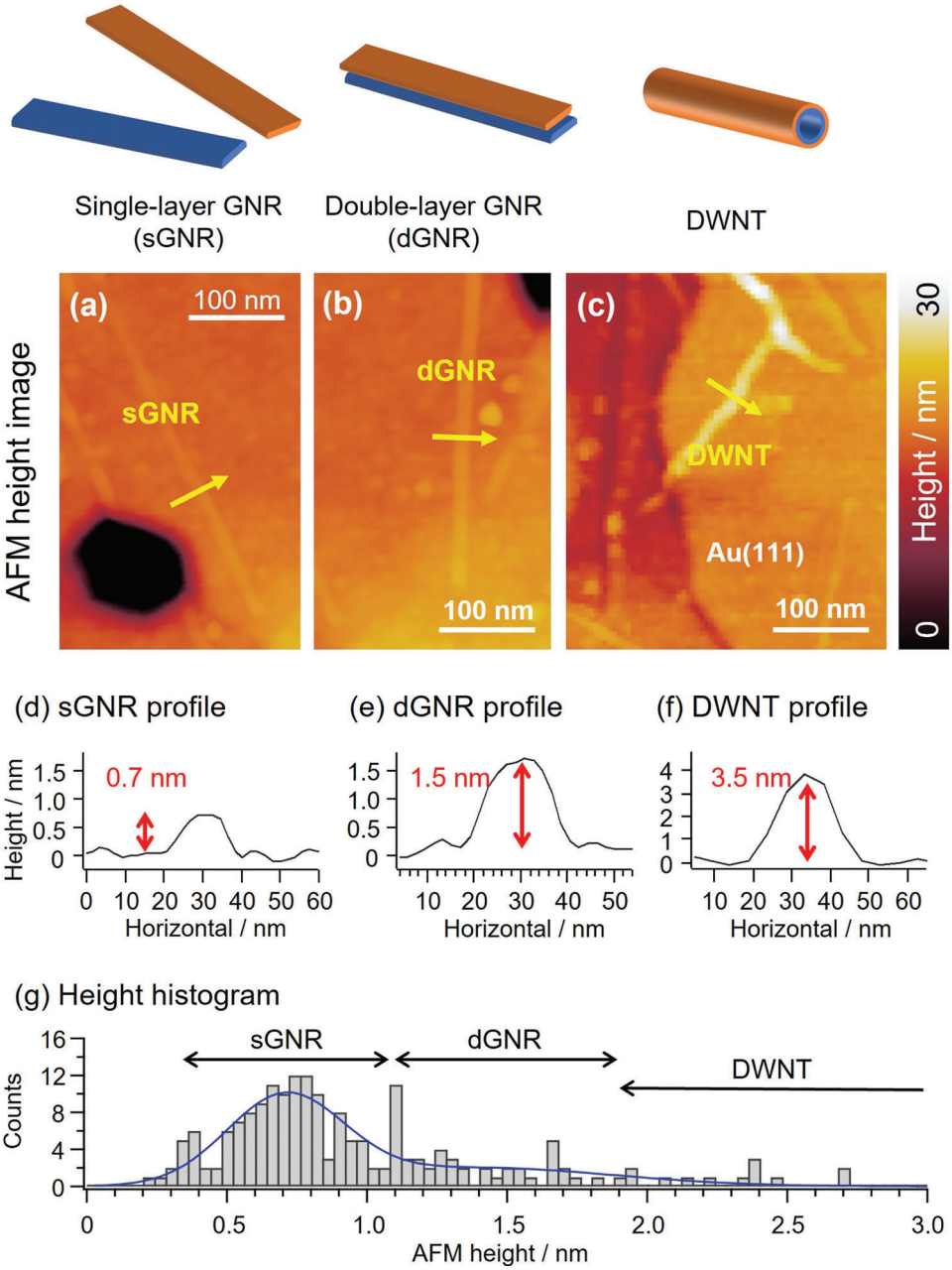


**Figure 1.** AFM characteristics of carbon nanostructures contained after unzipping process. a–c) Typical AFM height images of single-layer GNR (sGNR, (a)), double-layer GNR (dGNR, (b)), and double-walled carbon nanotube (DWNT, (c)) dispersed on Au(111) substrate. AFM images were obtained with silver nanowire TERS probes under tapping-mode AFM feedback. d–f) Corresponding cross-sectional height profiles of sGNR (d), dGNR (e), and DWNT (f). g) AFM height histogram of carbon nanostructures after 1 h unzipping ($n = 200$).

### 2.2. TERS Analysis on Y-Shaped GNRs

Next, we performed a TERS analysis, targeting GNRs, by applying a method to distinguish sGNR based on AFM height and nanoribbon width. Here, we mainly attempt to evaluate defect density of two sGNRs originating from the inner and outer DWNT walls, focusing on yGNRs. **Figure 2** shows TERS mapping images and averaged spectra on a yGNR. We performed hyperspectral mapping at 200 × 400 nm areas (with 10 nm pixel resolution). Peaks around 1330, 1600, and 2650 $cm^{-1}$ are, respectively, assigned to D-band (disorder-induced mode with one phonon lattice vibrational process), G-band ($E_{2g}$-symmetry phonon mode of $sp^2$ carbon atoms), and 2D-band (second-order mode of the D-band with two phonon lattice vibrational process).[40] Note that a nanometer-wide GNR's specific bands, such as radial breathing-like mode or shear-like mode, were not observed on the TERS spectra due to the larger width of our GNRs (10-40 nm).[41,42] Maps of D- and G-band peak intensity as well as D to G ratio (D/G) were generated by third polynomial peak fitting after baseline corrections in each data set. TERS

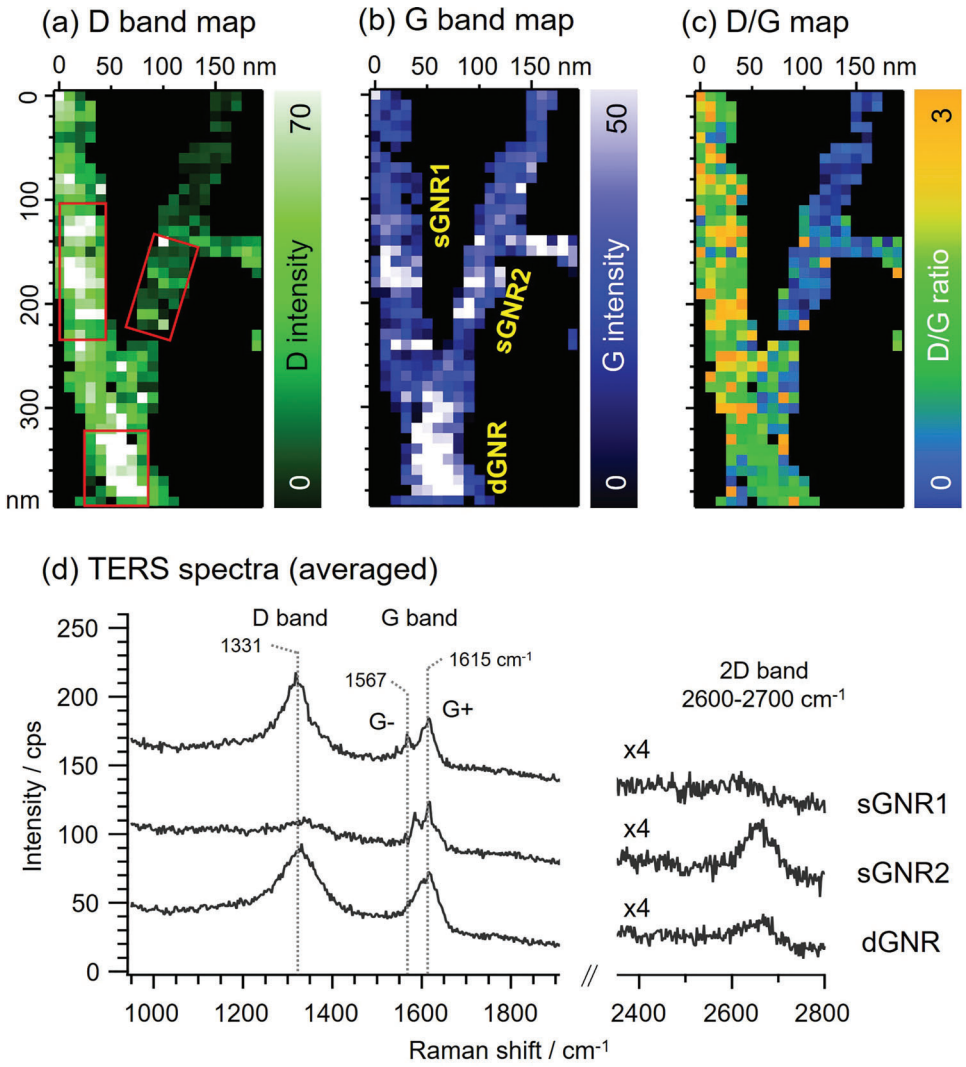


**Figure 2.** TERS measurements on a single y-shaped GNR (y-GNR: intermediate state of unzipping process) on Au(111) substrate. a–c) TERS-mapping images of D-band intensity (a), G-band intensity (b), and D/G ratio (c). The maps were obtained by hyperspectral TERS mapping performed under 632.8 nm excitation with the power of ≈40 kW $cm^{-2}$ (acquisition time: 300 ms per pixel). Mapping area was set to 200 × 400 nm with 10-nm pixel resolution. Maps were reconstructed from hyperspectral data sets by third polynomial peak–top fitting with linear baseline corrections on each spectrum. d) Averaged TERS spectra on sGNR1, sGNR2, and dGNR (named as (b)). Averaged area is indicated by red square in (a). Note that spectra at high frequency region (around 2D-band) were magnified by four times for easier visualization.

spectra in Figure 2d were extracted by averaging the collected spectra in the red square regions as shown in Figure 2a. Note that in this paper pixels below G-band intensity of 10 counts (= peak detection intensity threshold of the current mapping condition) are colored with black for easier visualization.

The corresponding AFM image of the TERS-mapped region is shown in Figure S3 (Supporting Information), from which we observed that sGNR1 (left, width 30 nm) is wider than sGNR2 (right, width 27 nm) and the height of dGNR (≈1.5 nm) is doubled to sGNRs. This suggests that sGNR1 and sGNR2 are branched from dGNR and originate from the outer and inner walls of an original DWNT, respectively. From TERS spectra in Figure 2d, we observed that the 2D-band of dGNRs consists of two Lorentzian components, while that of sGNRs showed a single component (Figure S4, Supporting Information). Note that a weak 2D-band of sGNR1 is due to higher defect density relative to sGNR2 as explained later. Generally, an asymmetric 2D-band in graphitic materials means that there is an interaction of the electronic states between graphene sheets.[43] This suggests that only dGNRs are bi-layer structures, in agreement with the AFM results. For sGNRs, we observed that the G-band was split into two peaks. The splitting of the G-band has been reported to be caused by the excitation of separate phonon modes for vibrations parallel (LO phonon mode, G+ band) and perpendicular (TO phonon mode, G- band) to the longitudinal axis.[41,44,45] This provides further evidence, in addition to the AFM topography data, that the measured structures are sGNRs. The D-band intensity was largely different between the two sGNRs (Figure 2d) and the maps in Figure 2a–c show the difference in D-band (D/G ratio), which is not local, but found across the ribbons. This

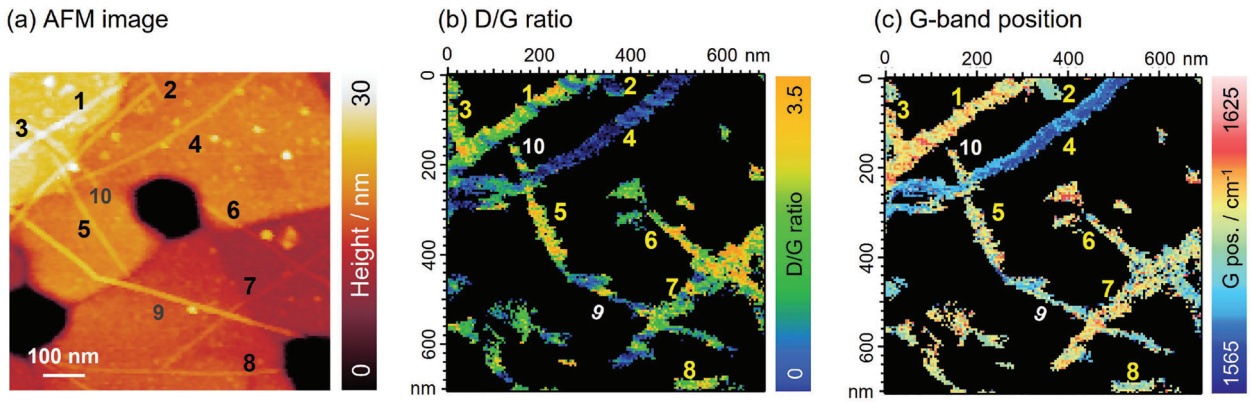


**Figure 3.** Large area TERS mapping. a) AFM height image of TERS-mapping region (700 × 700 nm). Note that ten carbon nanostructures (named 1–10) are located in the region and assignments of each carbon are summarized in Table 1. b,c) TERS-mapping images of D/G ratio (b) and G-band position (c) at the area of (a). TERS measurements were conducted under 632.8 nm excitation at 30 kW $cm^{-2}$ with 5-nm pixel resolution (acquisition time: 200 ms per pixel).

average D/G ratio was detected on the two sGNRs derived from another four yGNRs, with an averaged D/G ratio and ribbon width shown in Table S1 (Supporting Information). The D-band is a defect-induced carbon Raman mode activated by $sp^2$ carbon lattice disorder, and the D/G ratio has been widely utilized to assess chemical/physical defect densities on carbon materials.[46] In the case of GNRs, however, the D/G ratio may be altered not only by defect densities on a $sp^2$ plane but also by the types of edge structures due to GNR's higher surface area at edges relative to the $sp^2$ plane compared with graphene. This shows that a simple comparison of D/G ratios does not result in a direct comparison of defect densities on GNRs. Nonetheless, we found that the D/G ratio of sGNRs from the outer DWNT walls is higher than that of sGNRs from the inner DWNT walls in most cases (i.e., four out of five yGNRs, Table S1, Supporting Information), and that the D/G ratio of sGNRs from the outer DWNT walls is high on average (average D/G ≈1.4). As a result, assuming the randomness of the edge structure when unzipping, sGNR from the outer DWNT wall is presumed to be more defective than sGNR from the inner DWNT wall. More evidence can be found in 2D-band intensities. The intensity of the 2D-band is known to decrease with increasing defect density and becomes almost negligible on amorphous carbons such as graphene oxide.[40,47] Figure 2 shows that the 2D intensity of sGNR1 is significantly lower (and almost negligible) than that of sGNR2. Since 2D-band is still represented on defect-free zigzag-rich GNRs,[44] we conclude that sGNR1 (= outer wall) is substantially defected compared with sGNR2 (= inner wall). In conclusion, the GNRs unzipped from DWNT likely show a large difference in defect density depending on the origin of DWNT walls, that is, inner or outer.

### 2.3. Large-Scale TERS Mapping

Due to this, a large ribbon-to-ribbon spectral variety can be seen for unzipped sGNRs. **Figure 3** shows large area TERS maps of the D/G ratio (b) and the G-band peak position (c) and the corresponding AFM image (a). The mapping area was set to 700 nm × 700 nm and contained ten carbons structures. **Table 1** lists AFM heights and assignments, as well as the average D/G ratio and G-band peak position for each carbon numbered in the AFM image in Figure 3a. The D/G map in Figure 3b shows a large variation in the D/G ratio between sGNRs. For example, sGNR "2" and "4" showed a low D/G ratio of around 0.1–0.2, whereas sGNR "5" or "6" showed a D/G ratio higher than 2. Most GNRs exhibited some D/G heterogeneity along the ribbons, which may be due to point defects on the original DWNT that can be seen in "9" or inhomogeneities of edge structures along the ribbon. Overall, it appears that, in addition to the average differences in defect density related to the type of the DNWT wall (inner or outer), some local defects related to point defects originally present in the DWNT states, exist on unzipped sGNRs.

Furthermore, a large variety is also seen in the G-band peak position. The G-band peak position tends to show a higher frequency shift with increasing D/G ratio (Figure 3c), as reflected in the D/G to Pos(G) correlation plot in Figure S5 (Supporting Information). Similar spectral trends have been reported for defective graphene[47] and this suggests that the higher frequency shift is mainly due to the increased density of defects. However, we consider also another contribution to be included in the spectral variety, i.e., the edge effect. In particular, some GNRs (e.g., sGNR "1"

**Table 1.** List of AFM heights and assignments as well as average D/G ratio and G-band position of carbon structures numbered in Figure 3a.

| No. | Height [nm] | Assignment | D/G | Pos(G)/[$cm^{-1}$] |
|---|---|---|---|---|
| 1 | 0.84 | sGNR | 1.94 | 1602.2 |
| 2 | 0.67 | | 0.15 | 1590.3 |
| 3 | 0.83 | | 2.15 | 1599.0 |
| 4 | 0.78 | | 0.18 | 1576.8 |
| 5 | 0.91 | | 2.72 | 1596.9 |
| 6 | 0.59 | | 2.20 | 1587.2 |
| 7 | 0.64 | | 1.74 | 1591.6 |
| 8 | 0.79 | | 1.82 | 1592.9 |
| 9 | 2.34 | CNT | 1.07 | 1591.1 |
| 10 | 1.22 | dGNR | 1.75 | 1598.3 |

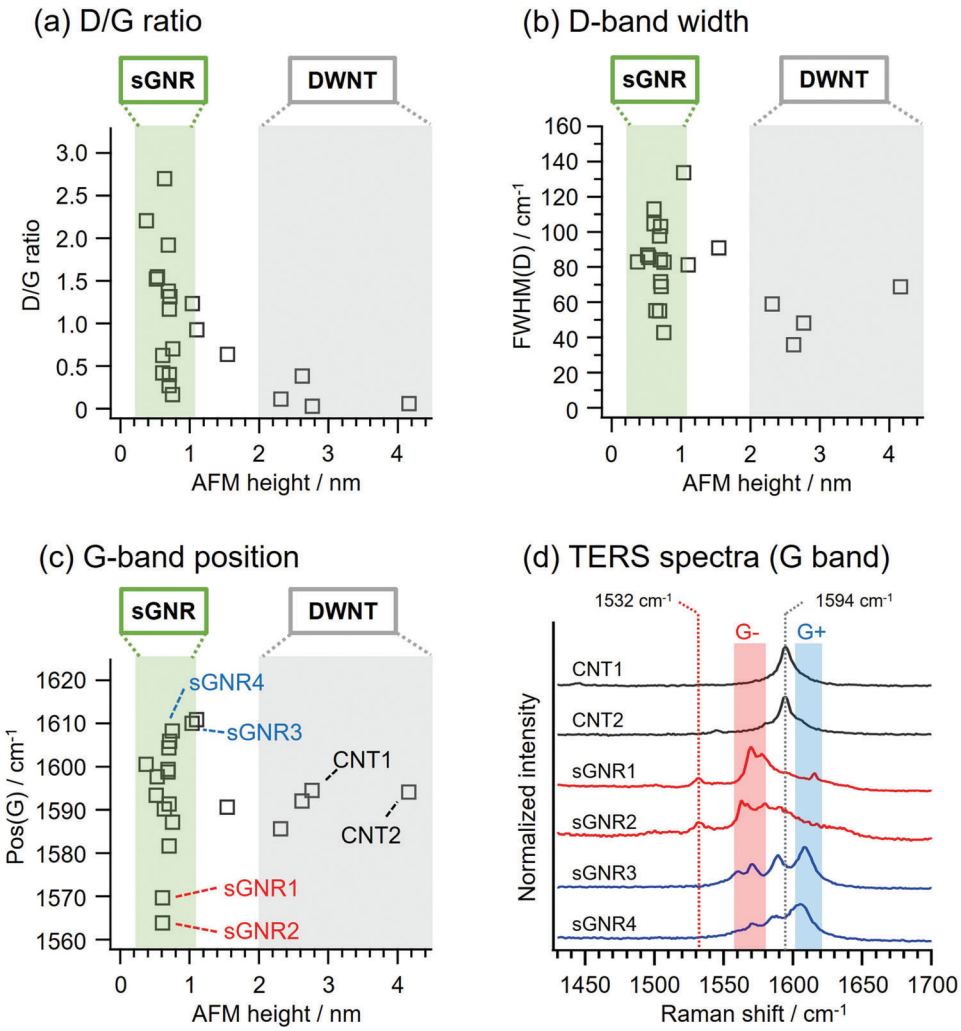


**Figure 4.** Statistical Raman parameter plot analyzed from TERS point spectra obtained from randomly selected 20 carbon structures. TERS point spectra and extracted Raman parameters are presented in Figure S6 and Table S2 (Supporting Information), respectively. a–c) Plots of D/G ratio (a), D-band width (b), and G-band position (c) as a function of AFM height. Note that carbons of less than 1 nm height are assigned to sGNRs, and larger than 2 nm are to DWNTs. d) G-band magnified TERS spectra of CNT 1–2 and sGNR 1–4 indicated in (c).

or "4") show a G-band peak position that exceeds the typical range of (nondoped) single-layer graphene, which is ≈1580–1600 $cm^{-1}$. Furthermore, there are variations in G-band position despite the similar D/G value (e.g., sGNR "3" and "6"). These trends cannot be simply explained by the difference in defect density, and indicate the presence of another structural contribution to the Raman spectra.

### 2.4. Heterogeneity on GNR Raman Parameters

To study in more detail the spectral variety observed on GNRs, TERS point spectra were measured from 20 carbon structures together with AFM images (Figure S6 and Table S2, Supporting Information), and the Raman parameters are plotted against the AFM height in **Figure 4**a–c. Instead of spectral mapping, point measurements (acquisition time: 10–30 s) were carried out to assure a high signal-to-noise ratio. This enables us to evaluate the peak width and the presence of minor peaks. The D/G ratio plot in Figure 4a represents the increase of as well as a large variety in the D/G ratio on GNRs, which is analogous to the mapping results in Figures 2–3. The D-band width (i.e., full width at half maximum of D-band, FWHM(D)) plotted in Figure 4b shows large variations (40–140 $cm^{-1}$), while for DWNTs the D-band width is ≈40–60 $cm^{-1}$. Considering that the D-band width correlates more directly to samples' crystallinity, the result suggests that there is a large ribbon-to-ribbon heterogeneity in defect density—from almost defect free to highly defective—on GNRs, likely due to the types of original DWNT walls described above (i.e., inner or outer).

The G-band position plot in Figure 4c shows a large variety on G-position after unzipping (see also Figure 3c). As already mentioned, the typical G-band position of (nondoped) single-layer graphene is in the range of 1580–1600 $cm^{-1}$, but in our experiments, some GNRs exceed this frequency range by 10 $cm^{-1}$ for both the lower and higher frequency. Although the extraordinal

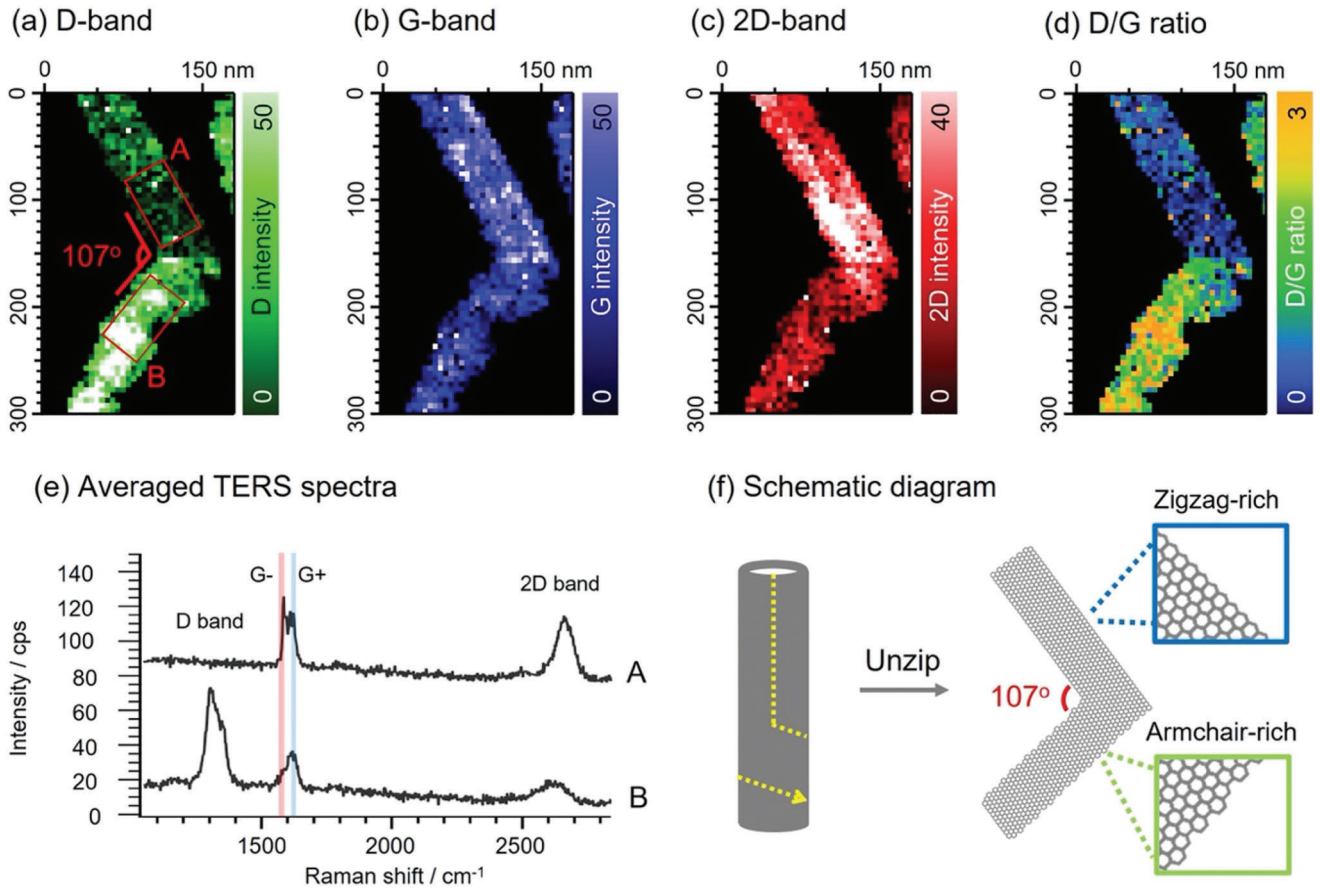


**Figure 5.** TERS measurements on an "irregularly" unzipped GNR. TERS mapping was conducted under the laser power of ≈40 kW $cm^{-2}$ with an integration time of 300 ms per pixel. Mapping area was set to 300 × 170 nm with 5-nm pixel resolution. a–d) TERS-mapping images of D-band intensity (a), G-band intensity (b), 2D-band intensity (c), and D/G ratio (d). e) Averaged TERS spectra of A and B marked with red square in (a). f) Schematic diagram of GNR structures.

variation of the G-band position may be due to the variations in strain[48] and/or carrier concentration,[49] we discuss the variation to be mostly caused by the variety of the GNR edge type based on the following detail spectrum analysis. TERS spectra of such "out of range" sGNRs (named sGNR 1–4) are plotted in Figure 4d. From the spectra, we found that the intensity ratio of G- and G+ are largely different between sGNR 1–2 and 3–4 and, interestingly, an additional peak at 1532 $cm^{-1}$ was observed on sGNR1 and 2. Referring to recent reports, it has been predicted that the G-band of GNRs splits into $G^-$ and $G^+$ depending on the edge structures, and $G^-$ and $G^+$ are activated only on Zigzag and Armchair edges, respectively.[45,24,50–51] Also, Hung et al. observed additional Raman bands at 1450 $cm^{-1}$ (very weak) and 1530 $cm^{-1}$ on graphene edges and discussed that those are associated with the edge phonon states of Armchair and Zigzag (H-terminated) edges, respectively.[52] According to these reports, GNR's Raman spectrum of Zigzag edges and Armchair edges should show a lower frequency-shifted G-band ($G^-$ active) with an edge phonon peak around 1530 $cm^{-1}$ and a higher frequency-shifted G-band ($G^+$ active) with a tiny peak around 1450 $cm^{-1}$, respectively, where most of the trends are seen on our sGNR1-2 and sGNR3-4. The absence of 1450 $cm^{-1}$ in TERS spectra of sGNR3 and sGNR4 could be due to the peak intensity being below the sensitivity limit due to the phonon band's intrinsically low intensity. Note that the D/G ratio is also known to be vastly different between Zigzag and Armchair edges, but in our case, the large ribbon-to-ribbon crystallinity variety made it difficult to discuss by D/G ratio (for this reason, we discussed the edge type by G-band shape). Therefore, we speculate that sGNR 1–2 and 3–4 have Zigzag-rich and Armchair-rich edge structures, respectively, and the sGNRs' large variety of G-band position is not only due to the variety of crystallinity but also to the large variation in GNR's edge structures, most likely due to the randomness of DWNT chirality as well as the nonchirality-specific unzipping nature.

Further complementary evidence of the edge variety in unzipped GNRs can be seen from an "irregularly" unzipped GNR (see TERS mapping shown in **Figure 5**). The measured sGNR exhibited changes in unzipped direction with an angle of about 107 degrees, where the point is assumed to be the connected part of two unzipping directions (a schematic is shown in Figure 5). The angle itself does not suggest a perfect zigzag-to-armchair configuration, but it should have structures with Zigzag-rich to Armchair-rich for either bottom/top part of the sGNR. An averaged TERS spectrum, extracted at the red square in the D-band map (marked A), in Figure 5e represents the top part showing a G-band split (G-active) with negligible D-band. This suggests that

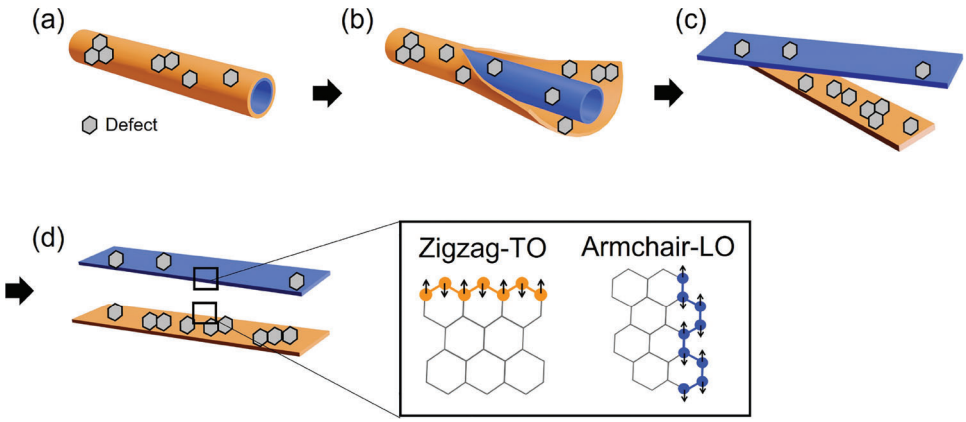


**Figure 6.** Schematic illustration of DWNT unzipping process. Initial heat treatment makes point defects on DWNT walls. Subsequent ultrasonic treatment initiates the cleavage of outer DWNT walls from initial defect points created by heat treatment (a). As the progress of the unzipping of the outer DWNT wall, the inner DWNT wall appears and initial defects are created on some area of the inner DWNT wall, and unzipping of this inner DWNT wall also begins (b). Defects continue to be created on the outer DWNT wall until the inner DWNT wall is completely unzipped resulting in lower crystallinity of sGNR originating from the outer DWNT wall (c). The edge structure of the obtained sGNR originating from both outer and inner DWNT are random (d).

the sGNR has high crystallinity (speculated to be generated from the inner wall), which allows us to also discuss the edge structures with the D/G ratio. The G-active nature suggests that the top part has Zigzag-rich structures, as discussed in Figure 4. While moving onto the bottom part (extracted from the red square marked B), we observe that the $G^-$ band is red-shifted ($G^+$ active) and, interestingly, the D/G ratio is suddenly increased up to about 3. Since the large D-band is previously reported for an Armchair-type graphene edges,[45] we speculate that the bottom part has Armchair-rich configuration.

### 2.5. Reaction Mechanisms of Chemical Unzipping

By combining the previous research with the current TERS results, the following reaction mechanism of the DWNT-unzipping process can be described (**Figure 6**). Our earlier work has shown that initial heat treatment causes a particular number of defects in DWNT and that subsequent ultrasonic treatment in the presence of PmPV initiates DWNT unzipping.[20] PmPV is required during the procedure because its phenylenevinylene structure aids in the production of a hydrogen or radical donor species via sonication.[22] Given the PmPV's molecular size, we predicted that it would predominantly adsorb on the surface (= outside wall) of DWNTs, and so causes defects preferentially on the outer walls of DWNTs (Figure 6a). The current TERS studies on intermediate yGNRs successfully produced complementary evidence of this, with a greater defect density seen on sGNRs from the outer DWNT wall than those from the inner wall (Figure 6b). Hence, these data support our hypothesis. As the reaction progresses, the inner DWNT wall begins to expose in the solution, and defects are generated via radical attack, possibly with a density significantly lower than the outer wall, and finally the inner DWNT wall cleavage occurs. During this stage, the defect density of GNRs from the outer wall may increase further. As a result, there is a significant difference in defect density between sGNRs originating from the outer and inner DWNT walls (Figure 6c). TERS microscopy has also revealed a wide range of variations in edge structure. We found that the sGNR edge structure is random and independent of the original wall types (= inner or outer). As a result, the unzipped GNRs contain edge structures ranging from Zigzag, Armchair to Chiral. This implies that the unzip reaction takes place in a nonchirality-specific manner (Figure 6d). Overall, our single GNR study using TERS microscopy provided deeper insights into the unzip reaction pathways that were previously unable to identify using conventional, averaged measurements.

## 3. Conclusion

In this contribution, we performed silver nanowire-based TERS analysis of DWNT-chemically unzipped GNR dispersed on Au(111). Graphitic Raman parameters were found to be largely different among GNRs and this suggests that unzipped GNRs possess ribbon-to-ribbon heterogeneity of graphitic/electronic structures. TERS measurements of a single y-shaped GNR (i.e., an intermediate state of the unzipping process) show that the large differences in defect density on unzipped GNRs are represented by the unzipping process, in which the inner wall of the DWNT is preserved to be nearly defect-free during the radical/oxidation reaction while the outer wall is highly defective. We also observed a "unique" spectral trend, which involves a split and notable shift in the G-band, as well as the appearance of a tiny peak at 1530 $cm^{-1}$, which we attribute to the edge phonon mode. This demonstrates that a variety of edge types, from Armchair to Zigzag, is present on unzipped GNRs. Therefore, we consider that the observed large variety on GNR Raman spectra arises from the heterogeneity of GNRs' defect density and edge structures, representing the characteristics and the randomness of the chemical unzipping reaction. Our single-GNR level work provides a better understanding of the reaction mechanism of chemical unzipping methods of DWNTs and would open possibilities for developing the next strategic design of chemically unzipping processes that leads to a practical large-scale synthesis of sGNRs with uniform qualities.

## 4. Experimental Section

*Sample Preparation*: Chemically unzipped GNRs from DWNTs were obtained by the previously reported procedure. Initial defects to start unzipping of DWNTs were created by annealing of DWNTs at 500 °C for 3 h. Then, the calcined DWNTs were unzipped into GNRs by 1 h sonication of suspension of annealed DWNTs in 1,2-dichloroethane containing poly(*m*-phenylenevinylene-*co*-2,5-dioctoxy-*p*-ohenylenevinylene) (PmPV). The obtained materials after the sonication were drop casted on Au(111) and AFM measurement was performed to characterize their topography. For this measurement, the obtained product was dispersed in dichloroethane and then drop-casted onto the Au(111) substrate and left it for 30 s, followed by washing of the substrate with acetone and ethanol. This operation was repeated ten times, and a sufficient amount of GNR was placed on the gold substrate for the measurement. The obtained substrate was immersed in chloroform for 15 min and then annealed at 350 °C for 90 min to remove excess amount of PmPV.

*Silver Nanowires*: Silver nanowires were synthesized following the previous reported procedure.[53] Briefly, 9.66 mL of EG was refluxed with 116.3 mg of PVP (0.108 M) at 160 °C for 1 h. Then, 80 µL of $CuCl_2$ in EG (4 mM) was added to this solution for 10 min. After adding 100 µL of $AgNO_3$ EG solution (0.12 M), the color of the solution turned from transparent to green. After 10 min, 4.9 mL of $AgNO_3$ EG solution (0.12 M) was added drop-wise with an injection rate of 100 µL $min^{-1}$. After adding all $AgNO_3$ solution, the reaction mixture was further refluxed at 160 °C for 1 h. Ethylene glycol (EG) solution containing 0.4% of water was used as a solvent through the reaction. Then, the mixture solution was washed with isopropanol by centrifuging the solution three times at 1200 rpm for 10 min to remove excess amount of PVP and EG. Finally, the precipitated AgNWs were dispersed in isopropanol.

*TERS Measurements*: TERS measurements were performed on an OmegaScope (Formerly AIST-NT, now Horiba) with a home-made optical platform. Laser light from a He–Ne laser (632.8 nm) was reflected by a dichroic mirror (Chroma, Z633RDC) and then focused onto the sample/tip by an objective (MITUTOYO, BD plan Apo 100x, N.A. 0.7). Raman scattering was collected using the same objective and directed to a CCD camera (Andor, Newton 920) equipped on a Raman spectrograph (Horiba JY, iHR-320) through the dichroic mirror, a pinhole, and a long pass filter (Chroma, HQ645LP). Polarization of incident light was set to maximize the TERS contrast/resolution (often parallel to the nanowire long axis). A stage was designed in house to hold the SPM unit at an angle of ≈60° (side-illumination) to the optical axis. Laser alignment to the tip apex was often done by recording Rayleigh scattering maps as the objective was scanned in the XY/XZ plane under a fixed tip position. Unless otherwise stated, TERS imaging was performed in a hybridized contact-mode (Spec-Top), in which TERS acquisition took place in contact-mode and the movement between pixels in tapping-mode. Measurements were carried out under ambient conditions and at room temperature. All SPM/Raman measurements were processed using Gwyddion/IGOR Pro software.

## Supporting Information

Supporting Information is available from the Wiley Online Library or from the author.

## Acknowledgements

This work was supported by the Research Foundation – Flanders (FWO) and the KU Leuven Research Fund (grant No. C14/15/053), and JSPS Kakenhi (grant Nos. JP19KK0136, JP20K05413 [to T.I.], JP22K20512 [to S.T.], JP18H01948 [to K.H]., JP21H04634, JP21K18871, JP21K18192, JP22H00328 [to H.U.], and JP19K22114 [to H.T.]). B.F. acknowledges the support from FWO for their postdoctoral fellowships (12 × 1419N and 12 × 1423N). P.W. acknowledges funding from the European Regional Development Fund and the programme Mobilitas Pluss (grant No. MOBJD609). Konica Minolta Foundation to T.I. is greatly acknowledged. This work was partially supported by JSPS Core-to-Core Program, A.

## Conflict of Interest

The authors declare no conflict of interest.

## Data Availability Statement

The data that support the findings of this study are available from the corresponding author upon reasonable request.

## Keywords

chemical unzipping, graphene nanoribbons, Raman scattering, silver nanowires, tip-enhanced Raman scattering

Received: March 2, 2023
Revised: August 4, 2023
Published online: August 30, 2023

[1] Z. H. Chen, Y. M. Lin, M. J. Rooks, P. Avouris, *Phys. E (Amsterdam, Neth.)* **2007**, *40*, 228.
[2] M. Y. Han, B. Ozyilmaz, Y. B. Zhang, P. Kim, *Phys. Rev. Lett.* **2007**, *98*, 206805.
[3] P. Wagner, C. P. Ewels, J. J. Adjizian, L. Magaud, P. Pochet, S. Roche, A. Lopez-Bezanilla, V. V. Ivanovskaya, A. Yaya, M. Rayson, P. Briddon, B. Humbert, *J. Phys. Chem. C* **2013**, *117*, 26790.
[4] Y. B. Hu, P. Xie, M. De Corato, A. Ruini, S. Zhao, F. Meggendorfer, L. A. Straaso, L. Rondin, P. Simon, J. Li, J. J. Finley, M. R. Hansen, J. S. Lauret, E. Molinari, X. L. Feng, J. V. Barth, C. A. Palma, D. Prezzi, K. Mullen, A. Narita, *J. Am. Chem. Soc.* **2018**, *140*, 7803.
[5] X. H. Zhou, G. Yu, *Adv. Mater.* **2020**, *32*, 1905957.
[6] V. Saraswat, R. M. Jacobberger, M. S. Arnold, *ACS Nano* **2021**, *15*, 3674.
[7] H. M. Wang, H. S. Wang, C. X. Ma, L. X. Chen, C. X. Jiang, C. Chen, X. M. Xie, A. P. Li, X. R. Wang, *Nat. Rev. Phys.* **2021**, *3*, 791.
[8] S. S. Datta, D. R. Strachan, S. M. Khamis, A. T. C. Johnson, *Nano Lett.* **2008**, *8*, 1912.
[9] L. Tapaszto, G. Dobrik, P. Lambin, L. P. Biro, *Nat. Nanotechnol.* **2008**, *3*, 397.
[10] L. Y. Jiao, L. Zhang, X. R. Wang, G. Diankov, H. J. Dai, *Nature* **2009**, *458*, 877.
[11] D. V. Kosynkin, A. L. Higginbotham, A. Sinitskii, J. R. Lomeda, A. Dimiev, B. K. Price, J. M. Tour, *Nature* **2009**, *458*, 872.
[12] L. Y. Jiao, X. R. Wang, G. Diankov, H. L. Wang, H. J. Dai, *Nat. Nanotechnol.* **2010**, *5*, 321.
[13] D. B. Shinde, J. Debgupta, A. Kushwaha, M. Aslam, V. K. Pillai, *J. Am. Chem. Soc.* **2011**, *133*, 4168.
[14] H. Shen, Y. Shi, X. Wang, *Synthetic Met.* **2015**, *210*, 109.
[15] J. M. Cai, P. Ruffieux, R. Jaafar, M. Bieri, T. Braun, S. Blankenburg, M. Muoth, A. P. Seitsonen, M. Saleh, X. L. Feng, K. Mullen, R. Fasel, *Nature* **2010**, *466*, 470.
[16] Z. Liu, S. Fu, X. Liu, A. Narita, P. Samorì, M. Bonn, H. I. Wang, *Adv. Sci.* **2022**, *9*, 2106055.
[17] Y. Zhang, J. Lu, Y. Li, B. Li, Z. Ruan, H. Zhang, Z. Hao, S. Sun, W. Xiong, L. Gao, L. Chen, J. Cai, *Angew. Chem., Int. Ed.* **2022**, *61*, e202204736.
[18] Z. Chen, A. Narita, K. Müllen, *Adv. Mater.* **2020**, *32*, 2001893.
[19] A. Morelos-Gomez, S. M. Vega-Dıaz, V. J. Gonzalez, F. Tristan-Lopez, R. Cruz-Silva, K. Fujisawa, H. Muramatsu, T. Hayashi, X. Mi, Y. Shi, H. Sakamoto, F. Khoerunnisa, K. Kaneko, B. G. Sumpter, Y. A. Kim, V. Meunier, M. Endo, E. Munoz-Sandoval, M. Terrones, *ACS Nano* **2012**, *6*, 2261.

 

[20] H. Tanaka, R. Arima, M. Fukumori, D. Tanaka, R. Negishi, Y. Kobayashi, S. Kasai, T. K. Yamada, T. Ogawa, *Sci. Rep.* **2015**, *5*, 12341.
[21] N. L. Rangel, J. C. Sotelo, J. M. Seminario, *J. Chem. Phys.* **2009**, *131*, 031105.
[22] M. Fukumori, S. Hara, T. Ogawa, H. Tanaka, *Jpn. J. Appl. Phys.* **2018**, *57*, 03ED01.
[23] W. W. Aji, Y. Usami, Hadiyawarman, R. O., H. Tanaka, *Appl. Phys. Express* **2020**, *13*, 101004.
[24] F. Negri, C. Castiglioni, M. Tommasini, G. Zerbi, *J. Phys. Chem. A* **2002**, *106*, 3306.
[25] A. C. Ferrari, *Solid State Commun.* **2007**, *143*, 47.
[26] L. G. Cancado, A. Jorio, E. H. Martins Ferreira, F. Stavale, C. A. Achete, R. B. Capaz, M. V. O. Moutinho, A. Lombardo, T. S. Kulmala, A. C. Ferrari, *Nano Lett.* **2011**, *11*, 3190.
[27] A. Eckmann, A. Felten, A. Mishchenko, L. Britnell, R. Krupke, K. S. Novoselov, C. Casiraghi, *Nano Lett.* **2012**, *12*, 3925.
[28] J. Chen, Y.-W. Huang, Y. Zhaob, *J. Raman Spectrosc.* **2015**, *46*, 64.
[29] J. Overbeck, G. B. Barin, C. Daniels, M. L. Perrin, L. Liang, O. Braun, R. Darawish, B. Burkhardt, T. Dumslaff, X.-Y. Wang, A. Narita, K. Müllen, V. Meunier, R. Fasel, M. Calame, P. Ruffieux, *Phys. Status Solidi B* **2019**, *256*, 1900343.
[30] J. Overbeck, G. B. Barin, C. Daniels, M. L. Perrin, O. Braun, Q. Sun, R. Darawish, M. De Luca, X.-Y. Wang, T. Dumslaff, A. Narita, K. Müllen, P. Ruffieux, V. Meunier, R. Fasel, M. Calame, *ACS Nano* **2019**, *13*, 13083.
[31] J. Stadler, T. Schmid, R. Zenobi, *Nanoscale* **2012**, *4*, 1856.
[32] T. Schmid, L. Opilik, C. Blum, R. Zenobi, *Angew. Chem., Int. Ed.* **2013**, *52*, 5940.
[33] Y. Fujita, P. Walke, S. De Feyter, H. Uji-i, *Jpn. J. Appl. Phys.* **2016**, *55*, 08NA02.
[34] Y. Fujita, P. Walke, S. De Feyter, H. Uji-i, *Jpn. J. Appl. Phys.* **2016**, *55*, 08NB03.
[35] S. Bonhommeau, S. Lecomte, *ChemPhysChem* **2018**, *19*, 8.
[36] P. Walke, Y. Fujita, W. Peeters, S. Toyouchi, W. Frederickx, S. De Feyter, H. Uji-i, *Nanoscale* **2018**, *10*, 7556.
[37] P. Walke, S. Toyouchi, M. Wolf, W. Peeters, S. R. Prabhu, T. Inose, S. De Feyter, Y. Fujita, H. Uji-i, *J. Phys. Chem. Lett.* **2018**, *9*, 7117.
[38] H. Wen, T. Inose, K. Hirai, T. Akashi, S. Sugioka, J. Li, W. Peeters, E. Fron, B. Fortuni, Y. Nakata, S. Rocha, S. Toyouchi, Y. Fujita, H. Uji-i, *Nanoscale* **2022**, *14*, 5439.
[39] H. Wen, J. Li, Q. Zhang, T. Inose, W. Peeters, B. Fortuni, H. Asakawa, A. Masuhara, K. Hirai, S. Toyouchi, Y. Fujita, H. Uji-i, *Nano Lett.* **2023**, *23*, 1615.
[40] J. B. Wu, M. L. Lin, X. Cong, H. N. Liu, P. H. Tan, *Chem. Soc. Rev.* **2018**, *47*, 1822.
[41] R. Gillen, M. Mohr, J. Maultzsch, *Phys. Rev. B* **2010**, *81*, 205426.
[42] I. A. Verzhbitskiy, M. De Corato, A. Ruini, E. Molinari, A. Narita, Y. Hu, M. G. Schwab, M. Bruna, D. Yoon, S. Milana, X. Feng, K. Müllen, A. C. Ferrari, C. Casiraghi, D. Prezzi, *Nano Lett.* **2016**, *16*, 3442.
[43] J.-C. Charlier, P. C. Eklund, J. Zhu, A. C. Ferrari, in *Carbon Nanotubes, Advanced Topics in the Synthesis, Structure, Properties and Applications*, (Eds: A. Jorio, G. Dresselhaus, M. S. Dresselhaus), Springer, Berlin, Heidelberg, Germany **2008**, p. 21.
[44] R. Yang, Z. Shi, L. Zhang, D. Shi, G. Zhang, *Nano Lett.* **2011**, *11*, 4083.
[45] J. Kim, N. Lee, Y. H. Min, S. Noh, N. K. Kim, S. Jung, M. Joo, Y. Yamada, *ACS Omega* **2018**, *3*, 17789.
[46] A. C. Ferrari, J. Robertson, *Phys. Rev. B* **2000**, *61*, 14095.
[47] J. Greenwood, T. H. Phan, Y. Fujita, Z. Li, O. Ivasenko, W. Vanderlinden, H. Van Gorp, W. Frederickx, G. Lu, K. Tahara, Y. Tobe, H. Uji-i, S. F. Mertens, S. De Feyter, *ACS Nano* **2015**, *9*, 5520.
[48] M. A. Bissett, M. Tsuji, H. Ago, *Phys. Chem. Chem. Phys.* **2014**, *16*, 11124.
[49] A. Das, S. Pisana, B. Chakraborty, S. Piscanec, S. K. Saha, U. V. Waghmare, K. S. Novoselov, H. R. Krishnamurthy, A. K. Geim, A. C. Ferrari, A. K. Sood, *Nature Nanotech.* **2008**, *3*, 210.
[50] C. Casiraghi, A. Hartschuh, H. Qian, S. Piscanec, C. Georgi, A. Fasoli, K. S. Novoselov, D. M. Basko, A. C. Ferrari, *Nano Lett.* **2009**, *9*, 1433.
[51] J. Laudenbach, B. Gebhardt, Z. Syrgiannis, F. Hauke, A. Hirsch, J. Maultzsch, *Phys. Status Solidi B* **2013**, *250*, 2687.
[52] Y. J. Hung, M. Hofmann, Y. C. Cheng, C. W. Huang, K. W. Chang, J. Y. Lee, *RSC Adv.* **2016**, *6*, 12398.
[53] K. E. Korte, S. R. Skrabalak, Y. Xia, *J. Mater. Chem.* **2008**, *18*, 437.